PHYSICAL REVIEW B **110**, 035142 (2024)

Emergent impervious band crossing in the bulk of the topological nodal-line semimetal $ZrAs_2$

A. S. Wadge,[1,*] K. Zberecki,[2,†] B. J. Kowalski,[3] D. Jastrzebski,[1,3,4] P. K. Tanwar,[1] P. Iwanowski,[3]
R. Diduszko,[3] A. Moosarikandy,[1] M. Rosmus,[5] N. Olszowska,[5] and A. Wisniewski[1,3]
[1]*International Research Centre MagTop, Institute of Physics, Polish Academy of Sciences, Aleja Lotnikow 32/46, PL-02668 Warsaw, Poland*
[2]*Faculty of Physics, Warsaw University of Technology, Koszykowa 75, Warsaw, 00-662, Poland*
[3]*Institute of Physics, Polish Academy of Sciences, Aleja Lotnikow 32/46, PL-02668 Warsaw, Poland*
[4]*Faculty of Chemistry, Warsaw University of Technology, Noakowskiego 3, 00-664 Warsaw, Poland*
[5]*National Synchrotron Radiation Centre SOLARIS, Jagiellonian University, Czerwone Maki 98, PL-30392 Cracow, Poland*

(Received 8 March 2024; revised 3 July 2024; accepted 8 July 2024; published 16 July 2024)

Topological nodal-line semimetals represent a unique class of materials with intriguing electronic structures and rich of symmetries, hosting electronic states with nontrivial topological properties. Among these, $ZrAs_2$ stands out, characterized by its nodal lines in a momentum space, governed by nonsymmorphic symmetries. This study integrates angle-resolved photoemission spectroscopy (ARPES) with density functional theory (DFT) calculations to explore the electronic states of $ZrAs_2$. Our study provides experimental evidence of nonsymmorphic symmetry-protected band crossing and nodal lines in $ZrAs_2$. In ARPES scans, we observed a distinctive surface and bulk states at different photon energies associated with nodal lines. Our results, supported by calculations based on DFT, unveil such impervious band crossing anchored at specific points in the Brillouin zone, with particular emphasis on the S point. Surface bands and bulk states near the crossing are elucidated through slab calculations, corroborating experimental findings. These findings enhance our understanding of the electronic structure of $ZrAs_2$.

DOI: 10.1103/PhysRevB.110.035142

I. INTRODUCTION

Topological semimetals (TSMs) represent a novel class of materials in condensed matter physics, distinguished by their unique electronic structures and the intricate role of symmetries. These materials are known for hosting electronic states that exhibit nontrivial topological properties [1–5]. In their electronic structure, the bands meet at certain isolated points or lines in the momentum space, giving rise to anomalous contribution to the physical properties, such as Shubnikov–de Haas oscillations, ultrahigh mobility, extremely large magnetoresistance, large anomalous Hall conductivity, etc. [6,7]. Angle-resolved photoemission spectroscopy (ARPES) plays a pivotal role in this research field by providing direct insight into the electronic band structures of the materials, enabling us to observe bulk and surface states and characterize symmetry-protected states [8–11].

Nodal-line semimetal is one of the types of TSMs where the conduction and valence bands intersect not at discrete points, but along a continuous loop in the momentum space, forming a one-dimensional "nodal line" (NL). NLs mark the presence of gapless bands, where two separate bands intersect accidently. The topological properties of accidental line nodes have an even codimension and lack absolute topological stability. However, by imposing certain symmetries, these line nodes can be stabilized, even if they are not necessarily positioned at the Fermi energy [12]. Hence observing the NL poses a challenging task for experiments. Nonsymmorphic symmetry, which involves a partial lattice shift combined with either a reflection (glide plane) or a rotation (screw axis), is sparsely seen in semimetals. The presence of nonsymmorphic symmetry only ensures the highly degenerate band crossings in the material which are resilient to spin-orbit interaction. The necessary condition to fix these crossings either at Γ point or at any high symmetry point is that material should possess nonsymmorphic symmetry as well as inversion symmetry [13–16].

Burkov *et al.* (2011) [12] presented a theoretical investigation of "nodal-semimetal" phases, specifically focusing on Weyl semimetals and line-node semimetals. Kim *et al.* (2015) [13] introduced a Z_2 class of topological semimetals characterized by Dirac line nodes (DLNs) in inversion-symmetric crystals. Fang *et al.* (2015) [14] studied two classes (with and without SOC) of three-dimensional TSMs with nodal lines protected by crystalline symmetries. Their theoretical contribution broadened the understanding of the role of crystalline symmetries in stabilizing nodal lines and suggested the potential for experiments [17–23].

In 2016, Schoop *et al.* [24] conducted a comprehensive theory and ARPES study on ZrSiS, revealing a Dirac cone protected by nonsymmorphic symmetry and the presence of three-dimensional Dirac lines. In the same year, Takane *et al.* [25] unearthed a Dirac node arc in the topological nodal-line semimetal HfSiS, a finding that emphasized the intricate nature and promising capabilities of HfSiS. Further advancements by Sims *et al.* [26] revealed surface states in HfP_2

---

[*] Contact author: wadge@magtop.ifpan.edu.pl

[†] Contact author: krzysztof.zberecki@pw.edu.pl

which vary depending on the material's termination. Bannies *et al.* [27] enhanced our knowledge through ARPES spectra studies on ZrP_2 in which bulk Fermi surface was observed on (001) orientation. Simultaneously, in the same year, Hao *et al.* [28] identified multiple Dirac nodal lines in $TaNiTe_5$, further broadening our perspective. Wu *et al.* [29] identified nonsymmorphic symmetry-protected band crossings in the square net metal $PtPb_4$. Mohanta *et al.* [30] and Fakherdine *et al.* [31] theoretically showed the nonsymmorphic symmetry protected semi-Dirac crossings fixed at the boundary of the Brillouin zone.

Zhou *et al.* [8] provided theoretical insights into nonsymmorphic symmetry and unprecedented butterflylike nodal lines with topological nature on the (010) plane of $ZrAs_2$. Additionally, our preliminary transport studies (Wadge *et al.* [32]) demonstrated pronounced Shubnikov–de Haas (SdH) oscillations above 9 T. The fast Fourier transform (FFT) of these SdH oscillations indicated the presence of two distinct bands at 195 and 682 T, suggesting the existence of two electronic pockets. Interestingly, a very recent study on magnetotransport has reported a significant SdH oscillation peak at 567 T, further underscoring the complexity and richness of the electronic structure of $ZrAs_2$ [33].

This study motivated an investigation into the band structure of $ZrAs_2$ using ARPES. Due to the natural cleavage of $ZrAs_2$ at the (001) plane, we focused our study on the band structure and corresponding ARPES for the (001) plane. This study reports the investigation of the electronic structure of single crystals of $ZrAs_2$. We demonstrated the Fermi surface using ARPES and DFT calculations. Additionally, we aimed to study nonsymmorphic symmetry-protected band crossing anchored at the *S* point in the band structure.

II. EXPERIMENTAL DETAILS

A. Single crystal growth and structural characterization

Single crystals of $ZrAs_2$ were grown using the two-stage chemical vapor transport (CVT) method, as shown in Fig. 1. Initially, polycrystalline $ZrAs_2$ was synthesized through the direct reaction of Zr sponge (Koch-Light Laboratories Ltd, 99.8%) and As (PPM Pure Metals, 99.999 995%) in an evacuated quartz ampoule. The ampoule was maintained for 7 days at 800 °C, with the other end kept at 460 °C to safely reduce the internal pressure. The resulting polycrystalline $ZrAs_2$ was pressed into pellets, loaded into a quartz tube with iodine (POCH, 99.8%, $10\,\mathrm{mg/cm^3}$ of ampoule volume) as transport agent, and sealed under vacuum. This assembly was then placed in a furnace with a temperature gradient of 700 °C (source zone) and 800 °C (crystallization zone) for 21 days. Afterward, the furnace was turned off and allowed to cool down to room temperature.

Crystal structure and crystallographic quality of grown $ZrAs_2$ were verified by x-ray powder diffraction using a Rigaku SmartLab 3kW diffractometer equipped with a tube having Cu anode, and operating with $U = 40$ kV and $I = 30$ mA. The characteristic peak positions were identified, as shown in Fig. 1(c), based on the data from International Centre for Diffraction Data (ICDD), Powder Diffraction File PDF-4+2023 RDB database.

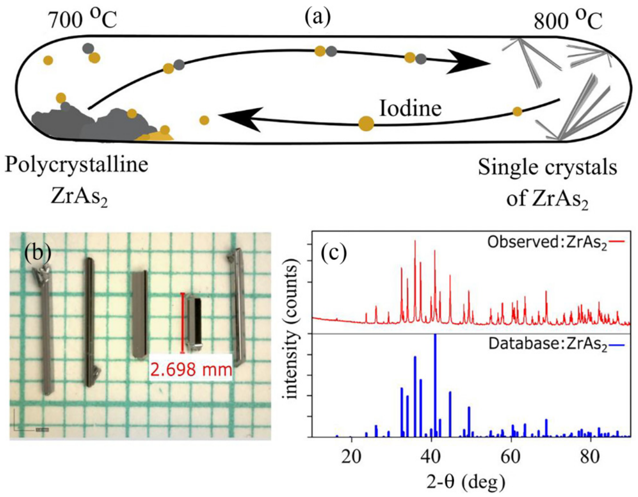

FIG. 1. (a) Schematic of the chemical vapor transport for $ZrAs_2$ synthesis, with source zone at 700 °C and growth zone at 800 °C, (b) needlelike $ZrAs_2$ single crystals obtained through the process, and (c) powder x-ray diffraction of the crystals.

For the quantitative chemical analysis of $ZrAs_2$, energy dispersive x-ray spectroscopy (EDX) was employed using a QUANTAX 400 Bruker system coupled with a Zeiss Auriga field-emission (Schottky-type) scanning electron microscope. The EDX measurements were conducted at 15 kV incident energy. The sample was prepared by sticking the crystals of $ZrAs_2$ on the carbon tape. Oriented samples were utilized, and the results confirmed the stoichiometric composition of $ZrAs_2$, with an atomic ratio of 1:2 (see Supplemental Material Fig. 1) [34], within the experimental error margin.

B. ARPES setup

Our experiment was conducted using the URANOS beamline at the National Synchrotron Radiation Centre SOLARIS in Krakow, Poland. The radiation source for our measurements was a quasiperiodic elliptically polarizing APPLE II type undulator, emitting photons in the energy range 8–170 eV.

The facility was equipped with a SCIENTA OMICRON DA30L photoelectron spectrometer. This spectrometer has a maximum detector resolution and angular resolution of 1.8 meV. However, the practical resolution depends on several factors such as the exit slit, photon energy, CFF, and pass energy. For this experiment, we achieved an energy resolution of 17 meV at 30 eV photon energy and 67 meV for 100 eV photon energy. The spectrometer also has an angular resolution of 0.1° and features deflectors that allow for wide-angle band structure measurements without repositioning the sample. This setup enabled us to perform precise band mapping across the entire Brillouin zone (BZ). ARPES spectra were obtained from single crystals that were freshly cleaved *in situ* within an ultrahigh vacuum (UHV) ($\sim 3.7 \times 10^{-11}$ torr) environment to obtain (001) surface, using different photon energies ranging 30–100 eV. During these measurements, the samples were consistently maintained at a temperature of

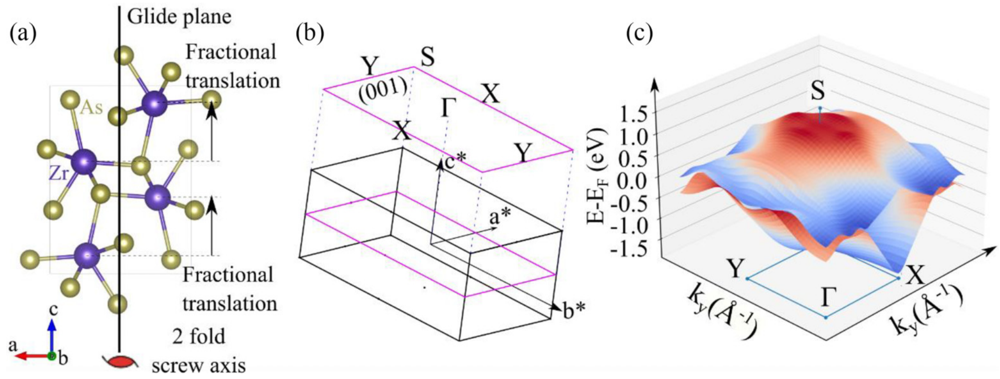

FIG. 2. (a) Crystal structure of $ZrAs_2$ showing nonsymmorphic symmetry with glide plane and twofold screw axis, (b) 3D Brillouin zone and projection on (001) plane with high symmetry points, (c) 3D visualization of the bands with SOC.

80 K. The analysis of the gathered ARPES data was conducted using IGOR PRO software and Python scripts.

III. DFT CALCULATION DETAILS

All the calculations were performed within density functional theory (DFT) as implemented in the VASP package [35–38] with projector augmented wave pseudopotential (PAW) [39,40], Perdew-Burke-Ernzerhof (PBE), and generalized gradient approximation (GGA) functionals [41]. For the sampling of the Brillouin zone, a dense $8 \times 8 \times 8$ grid was used, while the plane wave energy cutoff was set to 520 eV. All the structures were optimized until the force exerted on each ion was smaller than 10^{-5} eV/Å. Three-dimensional (3D) plots of Fermi surface were made with use of the XCrysDen code [42]. For further evaluation of the DFT results, the tight binding (TB) model was prepared with use of the WANNIER90 code [43]. This model was used to calculate surface states of the slab structure with use of the Wannier Tools package [44]. For the surface termination calculations, a $1 \times 1 \times 4$ supercell was employed, incorporating a 15 Å vacuum layer on top to model the surface. The total energy calculations indicated that "term. 2" was the most stable configuration.

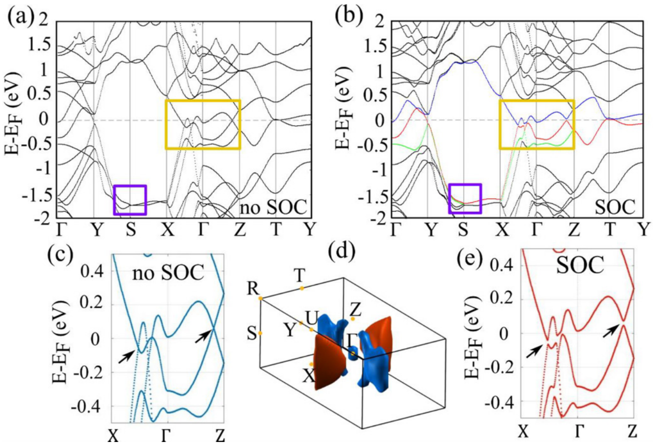

FIG. 3. Bulk band structures of $ZrAs_2$ calculated by density functional theory (DFT). (a) Band structure without spin-orbit coupling (SOC), showing accidental band crossings (yellow) and nonsymmorphic symmetry protected band crossings (purple). (b) Band structure with SOC. (c) Magnified view of the band structure along the X-Γ-Z path without SOC, highlighting the band crossings. (d) 3D Brillouin zone of $ZrAs_2$ showing electron pockets (blue) and hole pockets (red). (e) Magnified view along the X-Γ-Z path with SOC, demonstrating the gap opening due to SOC by arrows.

IV. RESULTS AND DISCUSSION

The CVT process produced needlelike single crystals of $ZrAs_2$ of average length 5–6 mm as shown in Fig. 1(b). X-ray diffraction analysis showed that $ZrAs_2$ crystallizes in an orthorhombic crystal structure with space group number 62 ($pnma$, D_{2h}). It is centrosymmetric in the nature with the refined

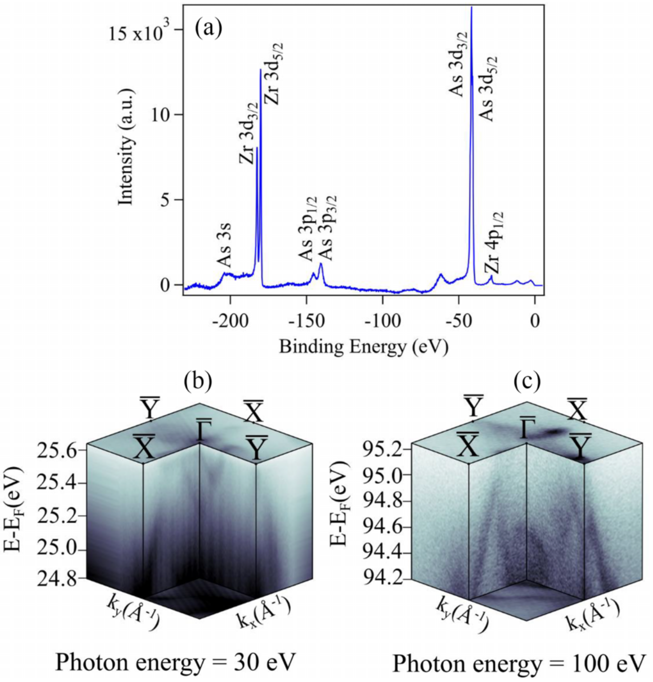

FIG. 4. (a) Core-level spectra of $ZrAs_2$ indicating Zr and As peaks confirming the only elements in $ZrAs_2$. 3D visualization of ARPES data for $ZrAs_2$ obtained at photon energies: (b) 30 eV and (c) 100 eV.

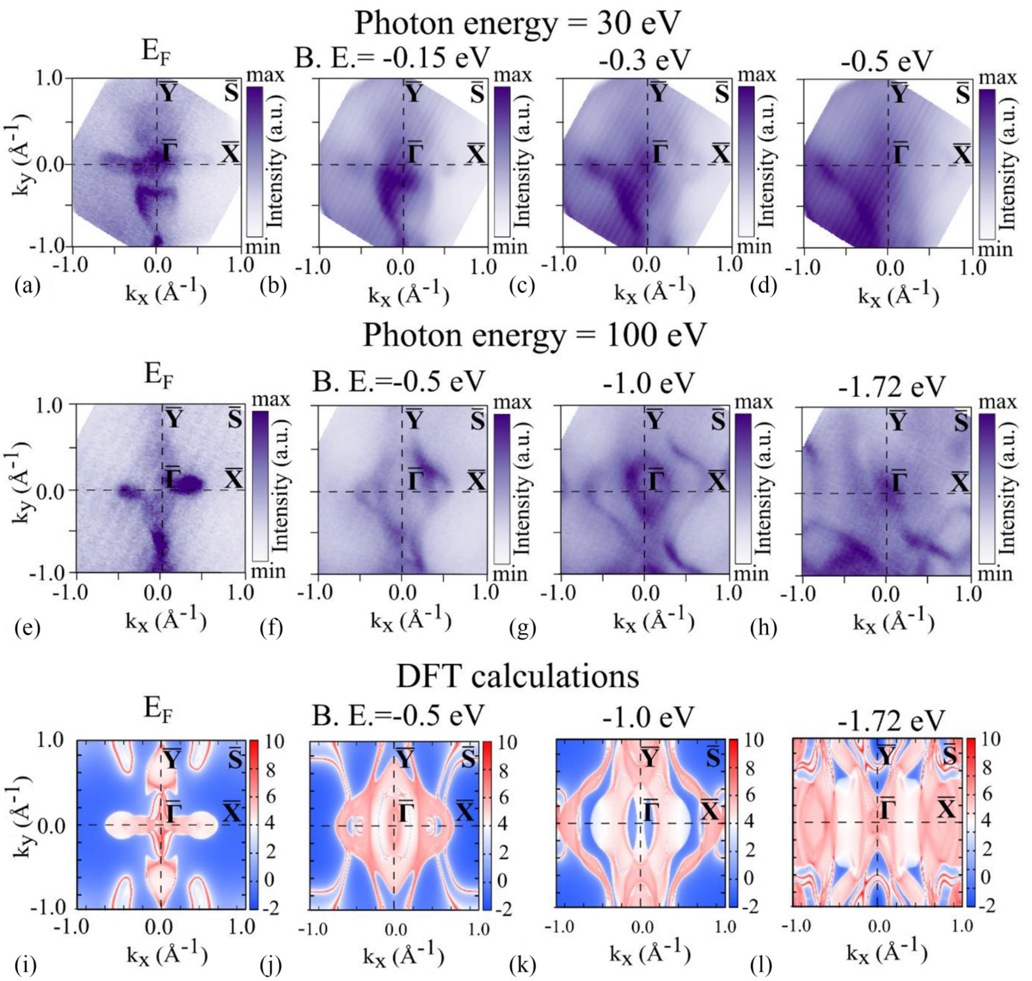

FIG. 5. The constant energy contours of $ZrAs_2$ at different binding energies obtained using ARPES. (a)–(d) Contours at 30 eV photon energy for binding energies: (a) E_F, (b) -0.15 eV, (c) -0.3 eV, and (d) -0.5 eV. (e)–(h) Comparison of constant energy contours at 100 eV photon energy with corresponding DFT-calculated constant energy contours for binding energies: (e), (i) E_F, (f), (j) -0.5 eV, (g), (k) -1.0 eV, and (h), (l) -1.72 eV.

lattice parameters $a = 6.801\,63(10)$ Å, $b = 3.688\,91(5)$ Å, $c = 9.030\,58(13)$ Å. In crystal structure of $ZrAs_2$, the Zr ion (blue) is surrounded by nine As ions (tan). It has nonsymmorphic symmetry with n glide plane perpendicular to ″a″ axis and twofold rotation screw axis [see Fig. 2(a)] [8]. The x-ray diffraction data confirm the single crystalline phase and are consistent with previous studies [33,45].

The lattice constants obtained through relaxation processes in computational simulations align closely with the values predicted by density functional theory (DFT). In Fig. 2(b), we present the (001) surface projection of the three-dimensional Brillouin zone, highlighting high symmetry points with Γ at the center. Figure 2(c) depicts a three-dimensional visualization of the electronic band structure, illustrating the dispersion of energy states across k_x and k_y momentum space.

DFT band structure calculations were performed both without and with the inclusion of SOC, as depicted in Figs. 3(a) and 3(b). The figures illustrate two distinct types of band crossings: accidental band crossings (ABCs), highlighted by a yellow rectangle, and nonsymmorphic symmetry-protected band crossings, highlighted by a purple rectangle. In the absence of SOC, band crossings can be observed along the X-Γ-Z path [see magnified bands for better visibility in Figs. 3(c) and 3(e)]. These crossings are disrupted and a gap of ∼20 meV emerges upon the inclusion of SOC. Conversely, the band crossings remain unaffected by SOC, as they are safeguarded from opening the gap by nonsymmorphic symmetry.

Figure 3(d) illustrates the 3D Brillouin zone with electron (blue) and hole (red) Fermi pockets. Unlike ZrP_2, $ZrAs_2$ lacks a third pocket associated with green band (hole-type) with the lowest energy [27]. Though ABC opens up the gap, which is very small, it preserves the semimetallic nature as described in Nandi *et al.* [33]. The bands near the Fermi level along the Γ-X path comprise a mix of As (p) and Zr (d) states, preventing assignment to specific ions (see Supplemental Material Fig. 8) [34].

The core-level spectrum was taken prior to ARPES measurements in order to check the composition and they showed the significant peaks of Zr $3d_{3/2}$ (181.1 eV), Zr $3d_{5/2}$ (178.8 eV), Zr $4p_{1/2}$ (28.5 eV), as well as As $3s$ (204.7 eV), As $3p_{1/2}$ (146.2 eV), As $3p_{3/2}$ (141.2 eV), As $3d_{3/2}$ (41.7 eV), and As $3p_{5/2}$ (41.7 eV), which are in good agreement [see Fig. 4(a)] with the binding energy database [45]. These peaks

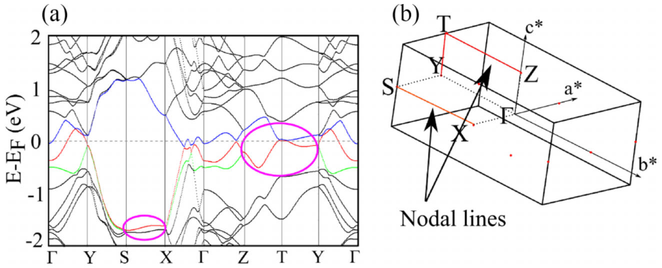

FIG. 6. (a) The bulk band structure in which nodal lines are indicated by magenta color ellipses, (b) the paths of nodal lines are shown in the Brillouin zone.

confirm the composition of Zr and As with no foreign quantity in the crystals.

We obtained ARPES spectra at various photon energies, with the most significant results observed at 30 and 100 eV [see Figs. 4(b) and 4(c)]. At higher photon energies, specifically 100 eV, we were able to map a more extensive portion of the Fermi surface, including the S points. In contrast, measurements at 30 eV revealed a smaller region of the Brillouin zone, which precluded the observation of the S point. Later, it turned out that ZrAs$_2$ naturally cleaves at the (001) plane with six possible terminations (Supplemental Material Figs. 5 and 6) [34].

Figures 5(a)–5(d) show the constant energy contours at a photon energy of 30 eV, illustrating the evolution from the Fermi level to a binding energy of $E_\mathrm{B} = -1.06$ eV at various binding energies. We have obtained ARPES at photon energies ranging 34−54 eV. As the photon energy changes, we observed shifts in the positions of several bands, indicating that these are likely bulk bands. In contrast, some bands at a binding energy of −0.5 eV remain stationary, suggesting they are surface states considering the overall spectra; the electronic structure is predominantly bulk in nature as shown in Supplemental Material Fig. 4 [34].

In addition, Figs. 5(e)–5(l) compare the constant energy contours at 100 eV photon energy with corresponding DFT-calculated contours for binding energies: (e) and (i) E_F, (f) and (j) −0.5 eV, (g) and (k) −1.0 eV, and (h) and (l) −1.72 eV. The theoretical constant energy contours were obtained for the semi-infinite slab with orientation (001). For $E = E_\mathrm{F}$, the electron and hole pockets [see Fig. 3(b)] can be clearly visible. Lowering the energy, the hole pocket shrinks, while the electron pocket becomes more robust. For $E_\mathrm{B} = -1.72$ eV in the vicinity of the S point one can observe the pronounced signatures of the Dirac crossings.

Figure 6 presents DFT analysis of the bulk band structure of ZrAs$_2$ and the characterization of its nodal lines. In Fig. 6(a), the bulk band structure is shown, with nodal lines highlighted by magenta ellipses along the X-S and Z-T-Y paths. Additionally, nodal lines are indicated in red within the 3D Brillouin zone. The path $\bar{Z}$-$\bar{T}$-$\bar{Y}$ is not observable in the ARPES results because the high-symmetry points Z and T are not present on the (001) plane. However, the nodal line along the $\bar{S}$-$\bar{X}$ path is clearly visible in Supplemental Material Figs. 3(a) and 3(b) [34].

Figures 7(a) and 7(e) shows the Fermi surface at photon energy 30 and 100 eV with all the high symmetry points. The cut along $\bar{X}$-$\bar{\Gamma}$-$\bar{X}$ reveals the band dispersion near the $\bar{\Gamma}$ point [see Figs. 7(b) and 7(c)], and the cut along $\bar{S}$-$\bar{Y}$-$\bar{S}$ is also shown. The consistency between these cross-sectional cuts and the slab calculations, displayed in Figs. 7(b) and 5(f) respectively, is notable.

Another important finding of our work is nonsymmorphic symmetry protected band crossings in the bulk. Nonsymmorphic symmetry alone ensures only the existence of band

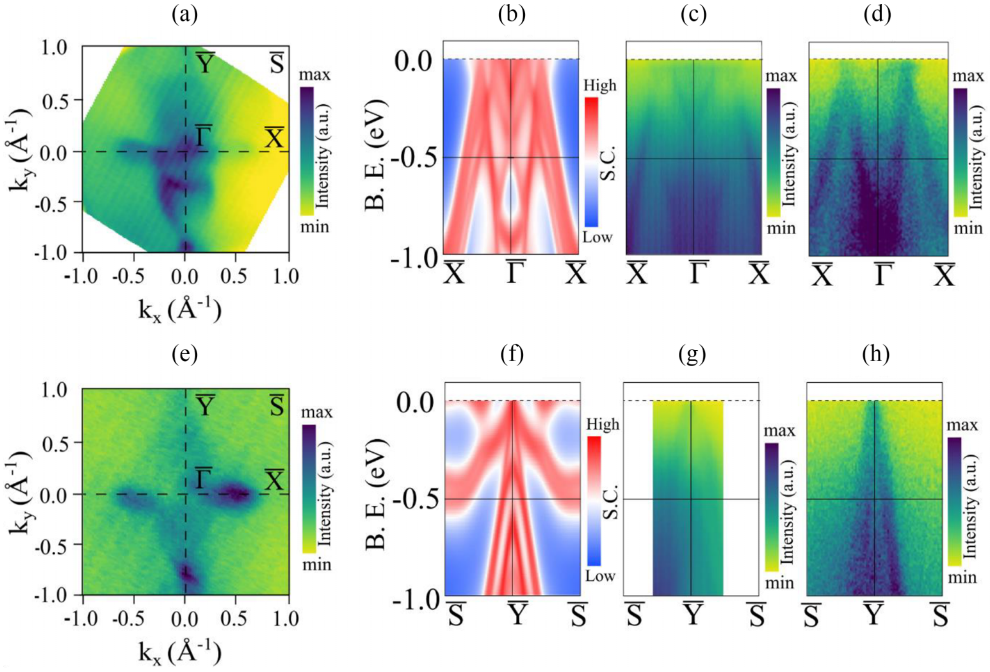

FIG. 7. (a), (e) ARPES reveals 2D Fermi surfaces at 30 and 100 eV photon energies. (b), (f) Theoretical band dispersion along $\bar{X}$-$\bar{\Gamma}$-$\bar{X}$ and $\bar{S}$-$\bar{Y}$-$\bar{S}$ paths. ARPES cuts at (c), (d) 30 eV and (g), (h) 100 eV photon energies, respectively.

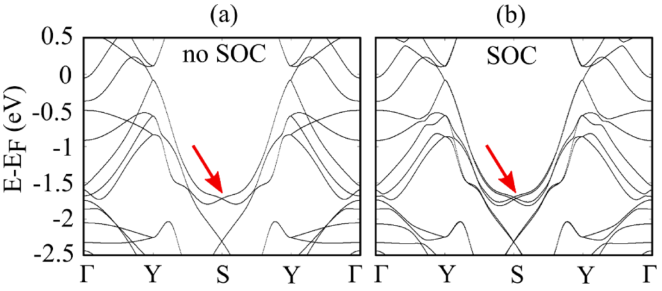

FIG. 8. Bulk band dispersion (a) without SOC and (b) with SOC along Γ-Y-S-Y-Γ showing Dirac band crossing (red arrow) at S point (−1.72 eV).

crossing in the band dispersion, yet it does not determine the specific location of this degenerate point in momentum space. However, the presence of inversion symmetry anchored the band crossing either at the $\bar{\Gamma}$ point or along the boundary of the Brillouin zone (BZ) [14]. Along with time reversal symmetry and inversion symmetry, ZrAs$_2$ shows nonsymmorphic symmetry. It has reflection with partial translation, $G = \{R|\vec{t}\}$, where G is glide symmetry, R is reflection and $\vec{t}$ is nonprimitive translation, and $S = \{C_2|\vec{t}\}$, where S is screw symmetry, and C_2 is twofold rotation.

The DFT-calculated bulk band dispersions, shown in Figs. 8(a) and 8(b), reveal that the band crossing at the $\bar{S}$ point exhibits fourfold degeneracy in the absence of spin-orbit coupling (SOC). Due to the protection of nonsymmorphic symmetry against SOC, there are twofold degenerate crossings at the $\bar{S}$ point ($E_B = -1.72$ eV), as illustrated in Fig. 8. The ARPES results presented in Figs. 9(a) and 9(b) confirm the presence of such band crossings at the $\bar{S}$ point. Additionally, various perpendicular cuts systematically demonstrate that at the $\bar{S}$ point, band crossings occur, and as the measurements move away from the $\bar{S}$ point, a gap begins to open. These observations are consistent with the DFT bulk and slab calculations shown in Figs. 9(c) and 9(d), providing a comprehensive understanding of the electronic structure. According to Zhou *et al.* [8], ZrAs$_2$ hosts topologically protected nodal lines consisting of concentric intersecting coplanar ellipses on the (010) plane whereas Nandi *et al.* [33] showed the nontrivial Berry phase from the transport measurements also on the (010) plane. Demonstrating the nontriviality of the bands on the naturally cleaved (001) plane is challenging because most of the surface and bulk bands overlap.

Although we have not yet obtained ARPES spectra on other cleavage planes, we have calculated the Fermi surfaces for the (100), (010), and (001) planes (see Supplemental Material Fig. 7) [34]. This opens up the possibility for more detailed ARPES studies on cleavage planes other than (001).

V. CONCLUSIONS

In this study, we comprehensively analyzed the electronic structure of ZrAs$_2$ using DFT calculations and ARPES measurements. Our observations revealed a 3D band structure characterized by electron and hole pockets, significantly influencing the material's electronic properties. The DFT calculations, including spin-orbit coupling, identified both accidental band crossings (ABCs) and nonsymmorphic symmetry protected band crossing.

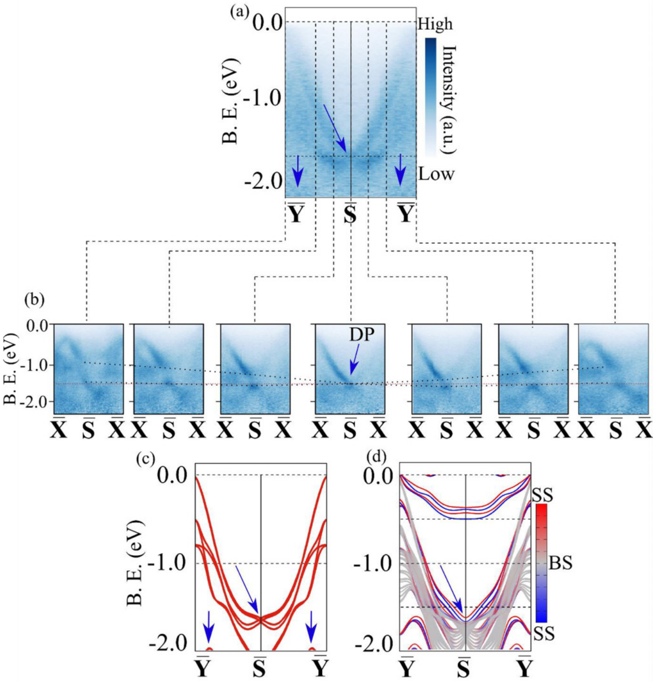

FIG. 9. (a) Illustrating potential Dirac-like crossings at the $\bar{S}$ points along the $\bar{Y}$-$\bar{S}$-$\bar{Y}$ path. (b) Multiple slices along the $\bar{X}$-$\bar{S}$-$\bar{X}$ direction, demonstrating band evolution across the $\bar{Y}$-$\bar{S}$-$\bar{Y}$ vector. (c), (d) Bulk band calculations and slab calculations along the $\bar{Y}$-$\bar{S}$-$\bar{Y}$ path (SS: surface states and BS: bulk states).

The ARPES data, obtained from *in situ* cleaving at the (001) plane, confirmed the presence of nodal lines along the $\bar{S}$-$\bar{X}$ path. Notably, we observed a nonsymmorphic symmetry-protected band crossing at $E_B = -1.72$ eV at the $\bar{S}$ point, indicating dominant bulk states. However, due to the cleaving at the (001) plane, we could not observe other parts of the nodal line along the $\bar{Z}$-$\bar{T}$-$\bar{Y}$ path.

This comprehensive investigation sheds light on the intricate electronic behavior of ZrAs$_2$ with the involved symmetries, important for fundamental understanding of nodal-line semimetals especially, and the critical role of nonsymmorphic symmetry in protecting band crossings at the S point. These insights could inform future research and potential applications in topological quantum materials and devices.

ACKNOWLEDGMENTS

We are grateful to B. Turowski for his invaluable assistance with ARPES cube data procedures, and to K. Cieslak for her support at the beamline. We thank C. Autieri, R. Bacewicz, S. Jatrzębski, and W. Paszkowicz for their insightful discussions. This research was supported by the Foundation for Polish Science project "MagTop" (Project No. FENG.02.01-IP.05–0028/23) cofinanced by the European Union from the funds of Priority 2 of the European Funds for a Smart Economy Program 2021–2027 (FENG). We acknowledge with appreciation the SOLARIS Centre for providing access to Beamline UARPES, where the crucial ARPES measurements were conducted. Additionally, we express our appreciation to Poland's high-performance infrastructure PLGrid, operated by Cyfronet AGH, for providing computational facilities and support under Computational Grant No. plgnanotrans10.

---

[1] C. Xu, J. Chen, G. X. Zhi, Y. Li, J. Dai, and C. Cao, Electronic structures of transition metal dipnictides XPn_2 (X = Ta, Nb; Pn = P, As, Sb), Phys. Rev. B **93**, 195106 (2016).

[2] Y. Shao, Z. Sun, Y. Wang, C. Xu, R. Sankar, A. J. Breindel, C. Cao, M. M. Fogler, A. J. Millis, F. Chou, Z. Li, T. Timusk, M. Brian Maple, and D. N. Basov, Optical signatures of Dirac nodal lines in $NbAs_2$, Proc. Natl. Acad. Sci. USA **116**, 1168 (2019).

[3] J. Chen, Y. K. Li, J. Dai, and C. Cao, Electronic structure and topological properties of centrosymmetric $MoAs_2/WAs_2$ from first principles, Sci. Rep. **7**, 10491 (2017).

[4] B. Wang, B. Singh, B. Ghosh, W. C. Chiu, M. M. Hosen, Q. Zhang, L. Ying, M. Neupane, A. Agarwal, H. Lin, and A. Bansil, Topological crystalline insulator state with Type-II Dirac fermions in transition metal dipnictides, Phys. Rev. B **100**, 205118 (2019).

[5] A. S. Wadge, G. Grabecki, C. Autieri, B. J. Kowalski, P. Iwanowski, G. Cuono, M. F. Islam, C. M. Canali, K. Dybko, A. Hruban, A. Łusakowski, T. Wojciechowski, R. Diduszko, A. Lynnyk, N. Olszowska, M. Rosmus, J. Kołodziej, and A. Wiśniewski, Electronic properties of $TaAs_2$ topological semimetal investigated by transport and ARPES, J. Phys.: Condens. Matter **34**, 125601 (2022).

[6] S. Li, Y. Liu, S. S. Wang, Z. M. Yu, S. Guan, X. L. Sheng, Y. Yao, and S. A. Yang, Nonsymmorphic-symmetry-protected hourglass Dirac loop, nodal line, and Dirac point in bulk and monolayer X_3SiTe_6 (X = Ta, Nb), Phys. Rev. B **97**, 045131 (2018).

[7] G. Cuono, C. Autieri, G. Guarnaccia, A. Avella, M. Cuoco, F. Forte, and C. Noce, Spin-orbit coupling effects on the electronic properties of the pressure-induced superconductor CrAs, Eur. Phys. J.: Spec. Top. **228**, 631 (2019).

[8] X. Zhou, C. H. Hsu, H. Aramberri, M. Iraola, C. Y. Huang, J. L. Manes, M. G. Vergniory, H. Lin, and N. Kioussis, Novel family of topological semimetals with butterflylike nodal lines, Phys. Rev. B **104**, 125135 (2021).

[9] H. Yang, A. Liang, C. Chen, C. Zhang, N. B. M. Schroeter, and Y. Chen, Visualizing electronic structures of quantum materials by angle-resolved photoemission spectroscopy, Nat. Rev. Mater. **3**, 341 (2018).

[10] B. Lv, T. Qian, and H. Ding, Angle-Resolved photoemission spectroscopy and its application to topological materials, Nat. Rev. Phys. **1**, 609 (2019).

[11] J. A. Sobota, Y. He, and Z. X. Shen, Angle-Resolved photoemission studies of quantum materials, Rev. Mod. Phys. **93**, 025006 (2021).

[12] A. A. Burkov, M. D. Hook, and L. Balents, Topological nodal semimetals, Phys. Rev. B **84**, 235126 (2011).

[13] Y. Kim, B. J. Wieder, C. L. Kane, and A. M. Rappe, Dirac line nodes in inversion-symmetric crystals, Phys. Rev. Lett. **115**, 036806 (2015).

[14] C. Fang, Y. Chen, H.-Y. Kee, and L. Fu, Topological nodal line semimetals with and without spin-orbital coupling, Phys. Rev. B **92**, 081201(R) (2015).

[15] Z. Wang, A. Alexandradinata, R. J. Cava, and B. A. Bernevig, Hourglass fermions, Nature (London) **532**, 189 (2016).

[16] H. Watanabe, H. C. Po, M. P. Zaletel, and A. Vishwanath, Filling-Enforced gaplessness in band structures of the 230 space groups, Phys. Rev. Lett. **117**, 096404 (2016).

[17] S.-S. Wang, Y. Liu, Z.-M. Yu, X.-L. Sheng, and S. A. Yang, Hourglass Dirac chain metal in rhenium dioxide, Nat. Commun. **8**, 1844 (2017).

[18] M. Rosmus, N. Olszowska, Z. Bukowski, P. Starowicz, P. Piekarz, and A. Ptok, Electronic band structure and surface states in Dirac semimetal $LaAgSb_2$, Materials (Basel) **15**, 7168 (2022).

[19] S. Y. Yang, H. Yang, E. Derunova, S. S. P. Parkin, B. Yan, and M. N. Ali, Symmetry demanded topological nodal-line materials, Adv. Phys. X **3**, 1414631 (2018).

[20] T. Nakamura, S. Souma, Z. Wang, K. Yamauchi, D. Takane, H. Oinuma, K. Nakayama, K. Horiba, H. Kumigashira, T. Oguchi, T. Takahashi, Y. Ando, and T. Sato, Evidence for bulk nodal loops and universality of Dirac-node arc surface states in $ZrGeX_c$ (X_c = S, Se, Te), Phys. Rev. B **99**, 245105 (2019).

[21] A. Topp, J. M. Lippmann, A. Varykhalov, V. Duppel, B. V. Lotsch, C. R. Ast, and L. M. Schoop, Non-Symmorphic band degeneracy at the Fermi level in ZrSiTe, New J. Phys. **18**, 125014 (2016).

[22] G. Cuono, F. Forte, M. Cuoco, R. Islam, J. Luo, C. Noce, and C. Autieri, Multiple band crossings and Fermi surface topology: Role of double nonsymmorphic symme-tries in MnP-type crystal structures, Phys. Rev. Mater. **3**, 095004 (2019).

[23] S. A. Ekahana, S.-C. Wu, J. Jiang, K. Okawa, D. Prabhakaran, C.-C. Hwang, S.-K. Mo, T. Sasagawa, C. Felser, B. Yan, Z. Liu, and Y. Chen, Observation of nodal line in non-symmorphic topological semimetal InBi, New J. Phys. **19**, 065007 (2017).

[24] L. M. Schoop, M. N. Ali, C. Straßer, A. Topp, A. Varykhalov, D. Marchenko, V. Duppel, S. S. P. Parkin, B. V. Lotsch, and C. R. Ast, Dirac cone protected by non-symmorphic symmetry and three-dimensional Dirac line node in ZrSiS, Nat. Commun. **7**, 11696 (2016).

[25] D. Takane, Z. Wang, S. Souma, K. Nakayama, C. X. Trang, T. Sato, T. Takahashi, and Y. Ando, Dirac-Node arc in the topological line-node semimetal HfSiS, Phys. Rev. B **94**, 121108(R) (2016).

[26] C. Sims, M. M. Hosen, H. Aramberri, C. Y. Huang, G. Dhakal, K. Dimitri, F. Kabir, S. Regmi, X. Zhou, T. R. Chang, H. Lin, D. Kaczorowski, N. Kioussis, and M. Neupane, Termination-Dependent topological surface states in nodal-loop semimetal HfP_2, Phys. Rev. Mater. **4**, 054201 (2020).

[27] J. Bannies, E. Razzoli, M. Michiardi, H. H. Kung, I. S. Elfimov, M. Yao, A. Fedorov, J. Fink, C. Jozwiak, A. Bostwick, E. Rotenberg, A. Damascelli, and C. Felser, Extremely large magnetoresistance from electron-hole compensation in the nodal-loop semimetal ZrP_2, Phys. Rev. B **103**, 155144 (2021).

[28] Z. Hao, W. Chen, Y. Wang, J. Li, X. M. Ma, Y. J. Hao, R. Lu, Z. Shen, Z. Jiang, W. Liu, Q. Jiang, Y. Yang, X. Lei, L. Wang, Y. Fu, L. Zhou, L. Huang, Z. Liu, M. Ye, D. Shen *et al.*, Multiple

Dirac nodal lines in an in-plane anisotropic semimetal, Phys. Rev. B **104**, 115158 (2021).

[29] H. Wu, A. M. Hallas, X. Cai, J. Huang, J. S. Oh, V. Loganathan, A. Weiland, G. T. McCandless, J. Y. Chan, S. K. Mo, D. Lu, M. Hashimoto, J. Denlinger, R. J. Birgeneau, A. H. Nevidomskyy, G. Li, E. Morosan, and M. Yi, Nonsymmorphic symmetry-protected band crossings in a square-net metal $PtPb_4$, npj Quantum Mater. **7**, 31 (2022).

[30] N. Mohanta, J. M. Ok, J. Zhang, H. Miao, E. Dagotto, H. N. Lee, and S. Okamoto, Semi-Dirac and Weyl fermions in transition metal oxides, Phys. Rev. B **104**, 235121 (2021).

[31] A. Fakhredine, R. M. Sattigeri, G. Cuono, and C. Autieri, Interplay between altermagnetism and nonsymmorphic symmetries generating large anomalous Hall conductivity by semi-Dirac points induced anticrossings, Phys. Rev. B **108**, 115138 (2023).

[32] A. S. Wadge, M. Ahmad, B. J. Kowalski, D. Jastrzębski, K. Zberecki, K. Dybko, P. Iwanowski, R. Diduszko, N. Olszowska, M. Rosmus, and A. Wiśniewski, *Investigation of Topological Nodal Line Semimetal: $ZrAs_2$*, ECOSS-36, 36th European Conference on Surface Science, 28 August–1 September 2023, Łódź, Poland.

[33] S. Nandi, B. B. Maity, V. Sharma, R. Verma, V. Saini, B. Singh, D. Aoki, and A. Thamizhavel, Magnetotransport and Fermi surface studies of a purported nodal line semimetal $ZrAs_2$, Phys. Rev. B **109**, 075155 (2024).

[34] See Supplemental Material at http://link.aps.org/supplemental/10.1103/PhysRevB.110.035142 for EDX spectrum, slab calculations, nodal line along S-X path, photon energy dependent ARPES spectra, termination dependent calculations, calculated Fermi surface on (001), (010), and (100) plane, and bulk band structure for Zr (d orbital) and As (p orbital) contributions.

[35] G. Kresse and J. Hafner, *Ab initio* molecular dynamics for liquid metals, Phys. Rev. B **47**, 558 (1993).

[36] G. Kresse and J. Hafner, *Ab Initio* molecular-dynamics simulation of the liquid-metalamorphous-semiconductor transition in germanium, Phys. Rev. B **49**, 14251 (1994).

[37] G. Kresse and J. Furthmüller, Efficiency of *ab-initio* total energy calculations for metals and semiconductors using a plane-wave basis set, Comput. Mater. Sci. **6**, 15 (1996).

[38] G. Kresse and J. Furthmüller, Efficient iterative schemes for *ab initio* total-energy calculations using a plane-wave basis set, Phys. Rev. B **54**, 11169 (1996).

[39] P. E. Blöchl, Projector augmented-wave method, Phys. Rev. B **50**, 17953 (1994).

[40] G. Kresse and D. Joubert, From ultrasoft pseudopotentials to the projector augmented-wave method, Phys. Rev. B **59**, 1758 (1999).

[41] J. P. Perdew, K. Burke, and M. Ernzerhof, Generalized gradient approximation made simple, Phys. Rev. Lett. **77**, 3865 (1996).

[42] http://www.xcrysden.org/.

[43] G. Pizzi, V. Vitale, R. Arita, S. Blügel, F. Freimuth, G. Géranton, M. Gibertini, D. Gresch, C. Johnson, T. Koretsune, J. Ibanez-Azpiroz, H. Lee, J. M. Lihm, D. Marchand, A. Marrazzo, Y. Mokrousov, J. I. Mustafa, Y. Nohara, Y. Nomura, L. Paulatto *et al.*, Wannier90 as a community Code: New features and applications, J. Phys.: Condens. Matter **32**, 165902 (2020).

[44] Q. S. Wu, S. N. Zhang, H. F. Song, M. Troyer, and A. A. Soluyanov, Wannier Tools: An open-source software package for novel topological materials, Comput. Phys. Commun. **224**, 405 (2018).

[45] P. E. R. Blanchard, R. G. Cavell, and A. Mar, On the existence of $ZrAs_2$ and ternary extension $Zr(Ge_xAs_{1-x})As$ ($0 \leqslant x \leqslant 0.4$), J. Alloys Compd. **505**, 17 (2010).